PERGAMON

International Journal of Heat and Mass Transfer 43 (2000) 4367–4379

International Journal of HEAT and MASS TRANSFER

www.elsevier.com/locate/ijhmt

Natural convection heat transfer in horizontal eccentric elliptic annuli containing saturated porous media

J.P.B. Mota[a,*], I.A.A.C. Esteves[a], C.A.M. Portugal[a], J.M.S.S. Esperança[a], E. Saatdjian[b]

[a] *Departamento de Química, Centro de Química Fina e Biotecnologia, Faculdade de Ciências e Tecnologia, Universidade Nova de Lisboa, 2825-114 Caparica, Portugal*

[b] *Laboratoire d'Energétique et de Méchanique Théorique et Appliquée, 2 Ave. de la Forêt de Haye, B.P. 160, 54504 Vandoeuvre Cedex, France*

Received 21 July 1999; received in revised form 21 February 2000

Abstract

The two-dimensional Darcy–Boussinesq equations, governing natural convection heat transfer in a saturated porous medium, are solved in generalised orthogonal coordinates, using high-order compact finites differences on a very fine grid. The mesh is generated numerically using the orthogonal trajectory method. The code is thoroughly validated against results reported in the literature for concentric and eccentric cylinders, obtained using different numerical techniques. The code is applied to horizontal eccentric elliptic annuli containing saturated porous media. The judicious stretching of one of the annular walls in the horizontal direction reduces the heat losses with respect to a concentric cylindrical annulus with the same amount of insulating material. The savings in heat transfer can be further improved if the elliptic annular shape is made eccentric. Previous studies show that, under certain conditions, eccentric cylinders may lead to a more effective insulation than concentric ones. The results presented here provide an alternative approach to optimising the heat transfer rate by a proper choice of the annular shape. The energy savings are of the order of 10%.

1. Introduction

Natural convection in porous annuli has a wide variety of technological applications involving thermal insulation, cryogenics, thermal energy storage, and underground cable systems, to mention just a few [1,2]. Nevertheless, despite its important industrial applications and the numerous studies published so far, it is a problem that is not yet totally understood. Previous published work has demonstrated, both experimentally and theoretically, the richness and complexity of the problem, which includes multiplicity of solutions (bifurcations [3–7] and hysteresis loops [8–10]), steady and periodic regimes [3,11], two- and three-dimensional flows [4,11,12], and various types of multicellular flow patterns [3,4,6,8,9].

Since the problem has been mostly studied in regular geometries, namely concentric and eccentric cylindrical and elliptic annuli, it lends itself to the application of different numerical techniques. These include finite differences [7–11,13], finite elements [11], spectral methods [3–5], perturbation expansion techniques [1,2], and boundary layer methods [14].

* Corresponding author. Tel.: +351-21-2954464; fax: +351-21-2948385.

E-mail address: pmota@dq.fct.unl.pt (J.P.B. Mota).

0017-9310/00/$ - see front matter
PII: S0017-9310(00)00068-5

The first experimental and numerical work on porous annuli was done by Caltagirone [11], who studied a concentric cylindrical porous layer with radius ratio $R = 2$. In his experiments, the thermal field was visualised using the Christiansen effect [15,16]. Experimental Nusselt numbers were also determined based on temperature measurements of the thermal field by means of several thermocouples inserted in the porous layer [17]. For Rayleigh numbers below 65 ± 5, Caltagirone observed a steady two-dimensional flow regime with two symmetric convective cells. For higher Rayleigh numbers, fluctuating three-dimensional effects were observed in the upper part of the layer, although the lower zone remained two-dimensional.

The visualisation experiments of Caltagirone have been recently redone by Charrier-Mojtabi et al. [6]. In a series of experiments on a cylindrical porous layer of $R = 2$, when the Rayleigh number was increased up to 250 (heating phase) the two-dimensional flow consisting of two symmetric cells became three-dimensional in the upper part of the layer, while still remaining two-dimensional in the lower part. During the cooling phase the flow became two-dimensional again, but this time four cells appeared in the layer. The original two-cellular flow became visible again when the Rayleigh number dropped below 69. This set of experiments is very interesting, since it proves the existence of a two-dimensional flow.

The observation that reducing the radius ratio defers the convective effects to higher Rayleigh numbers has led to the study of eccentric cylinders, since they may lead to a reduction of the heat losses with respect to the concentric case. Moving the inner cylinder upwards, so that its centre is above that of the outer cylinder, decreases the local thickness of the upper part of the annulus, where the convective effects are stronger, therefore reducing the impact of the convective heat transfer. On the other hand, the decrease of gap spacing in the top part of the layer increases the conductive heat losses. Hence, one may expect that an optimal value of the eccentricity exists for which the heat losses are minimised. This problem was first studied by Bau et al. using both finite differences [18] and regular perturbation expansion techniques [1,2]. Although the results presented apply to small Rayleigh numbers only, it is concluded in those works that the heat losses can be reduced with respect to the concentric case. In a later study, Himasekhar and Bau [14] used a boundary-layer technique to obtain a correlation for the Nusselt number, which is valid for a large range of Rayleigh numbers and geometric parameters. The above-mentioned studies were restricted to the simplest flow regime, which is the two-dimensional two-cellular one.

More recently, Mota and Saatdjian [7] extended the study of eccentric cylinders to four-cellular flow conditions and observed that the eccentricity that minimises the heat transfer for a given Rayleigh number and radius ratio changes with the flow regime. As a more robust alternative to setting the eccentricity equal to the value that minimises the heat transfer in two-cellular flow conditions, the authors proposed increasing the eccentricity up to the value above which the four-cellular flow regime is no longer physically possible.

Here, the two-dimensional Darcy–Boussinesq equations are solved in generalised orthogonal coordinates using a high-order finite difference method. In principle, any annular geometry can be handled with this code if an orthogonal coordinate transformation that maps the physical domain onto a rectangle is known. In order to reduce the work of adapting the code to a particular geometry, the grid is generated numerically. In practice, when studying the impact of geometry on heat transfer, the code must be applied to a family of shapes defined by a limited number of parameters, otherwise the analysis is not manageable. An eccentric elliptic annulus, symmetric with respect to the vertical centre-plane, was selected since very different annular shapes can be obtained through a proper selection of the values of the geometric parameters.

Since in most studies symmetry about the vertical centre-plane is assumed in the numerical model or observed experimentally, the total number of flow cells

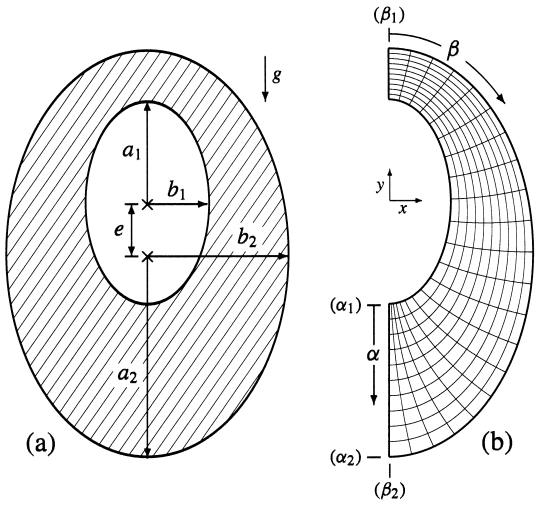

Fig. 1. (a) Geometrical configuration of the problem; (b) sketch of the computational domain and orthogonal coordinate system (α, β) for an annular space defined by $\Omega_1 = 0.6$, $\Omega_2 = 0.7$, $R = 2$, and $\epsilon = 0.55$. Also included in the figure is the numerical grid generated using the orthogonal trajectory method. The actual grid employed in the simulations has 161 $\times$ 101 ($\alpha \times \beta$) points, although for clarity purposes only a few grid lines are drawn.

in the annular space is always even. For this reason, some authors characterise the flow field by counting the number of cells in half the annular space, while others count the total number of cells. This may eventually confuse the reader if it is not clearly stated in the text what part of the layer is effectively taken into account. In this paper we always refer to the total number of cells in the layer.

2. Problem formulation

The annular space between two vertically aligned eccentric ellipses, as depicted in Fig. 1(a), is completely defined by the following dimensionless parameters: the axes ratio of each ellipse,

$$\Omega_1 = b_1/a_1 \quad \text{and} \quad \Omega_2 = b_2/a_2; \tag{1}$$

the hydraulic-radius ratio,

$$R = R_2/R_1 = \sqrt{\Omega_2/\Omega_1}(a_2/a_1) = \sqrt{\Omega_1/\Omega_2}(b_2/b_1), \tag{2}$$

where $R_1 = \sqrt{a_1 b_1}$ and $R_2 = \sqrt{a_2 b_2}$; and the relative eccentricity,

$$\epsilon = e/(R_2 - R_1). \tag{3}$$

For example, given a_1, the other axes can be calculated using the following expressions:

$$b_1 = \Omega_1 a_1, \quad a_2 = R\sqrt{\Omega_1/\Omega_2}a_1, \qquad b_2 = \Omega_2 a_2 = R\sqrt{\Omega_1\Omega_2}a_1. \tag{4}$$

The eccentricity is denoted as positive when the centre of the inner ellipse is above the centre of the outer ellipse. The geometric parameters employed in this work follow, as close as possible, the nomenclature adopted by most authors who have studied concentric and eccentric cylinders.

The problem is formulated as follows. The annular space is occupied by a saturated porous medium. The surfaces of the two ellipses are held at constant temperatures, T_1' and T_2', respectively, with $T_1' > T_2'$. The following assumptions are made in order to simplify the formulation:

- the fluid is in thermal equilibrium with the porous matrix;
- the porous medium is assumed to be macroscopically homogeneous and isotropic, and is treated as a fictitious fluid with heat capacity $(\rho C_p)_e = \varepsilon(\rho C_p)_f + (1-\varepsilon)(\rho C_p)_s$ and effective thermal conductivity k_e;
- the physical properties of the fluid are evaluated at the mean temperature $T_m' = (T_1' + T_2')/2$, and are considered constant;
- the flow in the porous medium is assumed to be governed by Darcy's law;
- density variations with temperature are only taken into account in the buoyancy terms (Boussinesq approximation).

These assumptions are a valid approximation for a large range of practical applications, as demonstrated by Aniri and Vafai [19]. Given the preceding assumptions, the governing dimensional equations in vector form can be written as

$$\nabla' \cdot \boldsymbol{v}' = 0, \tag{5}$$

$$\boldsymbol{v}' = -\frac{\lambda}{\mu}\left(\nabla' P' - \rho \boldsymbol{g}\right), \tag{6}$$

$$\left(\rho C_p\right)_e \frac{\partial T'}{\partial t'} + \left(\rho C_p\right)_f \boldsymbol{v}' \cdot \nabla' T' - k_e \nabla^2 T' = 0, \tag{7}$$

$$\rho = \rho_m\left[1 - \gamma\left(T' - T_m'\right)\right]. \tag{8}$$

These equations represent, respectively, the continuity equation for an incompressible fluid, Darcy's law for steady-state flow in a porous medium, the energy equation, and the fluid equation of state. The reader is referred to the nomenclature section for the meaning of those symbols that are not explicitly defined in the text.

Eqs. (5)–(8) are rendered non-dimensional by making use of the following dimensionless variables, in which R_1 is taken as the reference length:

$$(x, y) = \frac{\left(x', y'\right)}{R_1}, \quad t = \frac{k_e}{R_1^2\left(\rho C_p\right)_e}t', \qquad \boldsymbol{v} = \frac{R_1\left(\rho C_p\right)_f}{k_e}\boldsymbol{v}', \quad T = \frac{T' - T_2}{T_1 - T_2}, \qquad P = \frac{\left(\rho C_p\right)_f \lambda}{k_e \mu}P'. \tag{9}$$

In the scaled coordinate space, the axes of the ellipses have the following dimensionless values:

$$A_1 = 1/\sqrt{\Omega_1}, \quad B_1 = \sqrt{\Omega_1}, \quad A_2 = R/\sqrt{\Omega_2}, \qquad B_2 = R\sqrt{\Omega_2}. \tag{10}$$

Since the flow is assumed to be two-dimensional and incompressible, a dimensionless stream function, ψ, is defined as

$$\nabla\psi = -\mathbf{e}_z \times \boldsymbol{v}, \tag{11}$$

so that the continuity equation is automatically satis-

fied. The symbol $\mathbf{e}_z$ denotes the Cartesian unit vector normal to the cross section of the annular layer. Taking the curl of Eq. (6) and retaining the z component, replaces pressure by ψ as dependent variable. This formulation has been employed with success by several authors [6–9,11,20,21]. The resulting governing set of dimensionless equations reduces to

$$\frac{\partial T}{\partial t} = \nabla^2 T - \boldsymbol{v} \cdot \nabla T, \tag{12}$$

$$\nabla^2 \psi = -Ra\left(\boldsymbol{e}_y \times \nabla T\right) \cdot \boldsymbol{e}_z. \tag{13}$$

The dimensionless parameter appearing in Eq. (13) is the Darcy–Rayleigh number based on the inner hydraulic radius. It is defined by

$$Ra = \frac{\left(\rho C_p\right)_f \lambda \rho_m g \gamma (T_1 - T_2) R_1}{k_e \mu}. \tag{14}$$

The problem is solved in generalised orthogonal coordinates, although, as stated above, the discussion is restricted to eccentric elliptic annuli. Orthogonal coordinates are adopted here, since they produce fewer additional terms in the transformed partial differential equations and have the advantage that the boundary conditions are represented entirely along coordinate lines without the need of interpolation [22].

When the 2D Cartesian space (x, y) is mapped onto an orthogonal space defined by the set of coordinates (α, β), Eqs. (12) and (13) take the following form:

$$\frac{\partial T}{\partial t} = \frac{1}{h_\alpha h_\beta}\left[\frac{\partial}{\partial \alpha}\left(\frac{h_\beta}{h_\alpha}\frac{\partial T}{\partial \alpha}\right) + \frac{\partial}{\partial \beta}\left(\frac{h_\alpha}{h_\beta}\frac{\partial T}{\partial \beta}\right)\right] - \left(\frac{v_\alpha}{h_\alpha}\frac{\partial T}{\partial \alpha} + \frac{v_\beta}{h_\beta}\frac{\partial T}{\partial \beta}\right), \tag{15}$$

$$\frac{\partial}{\partial \alpha}\left(\frac{h_\beta}{h_\alpha}\frac{\partial \psi}{\partial \alpha}\right) + \frac{\partial}{\partial \beta}\left(\frac{h_\alpha}{h_\beta}\frac{\partial \psi}{\partial \beta}\right) = Ra\left(\frac{\partial y}{\partial \beta}\frac{\partial T}{\partial \alpha} - \frac{\partial y}{\partial \alpha}\frac{\partial T}{\partial \beta}\right), \tag{16}$$

where v_α and v_β are given by

$$v_\alpha = -\frac{1}{h_\beta}\frac{\partial \psi}{\partial \beta}, \qquad v_\beta = \frac{1}{h_\alpha}\frac{\partial \psi}{\partial \alpha}. \tag{17}$$

The metric coefficients associated with the coordinate transformation are defined by

$$h_\alpha = \sqrt{\left(\frac{\partial x}{\partial \alpha}\right)^2 + \left(\frac{\partial y}{\partial \alpha}\right)^2}, \qquad h_\beta = \sqrt{\left(\frac{\partial x}{\partial \beta}\right)^2 + \left(\frac{\partial y}{\partial \beta}\right)^2}. \tag{18}$$

In the orthogonal grid employed in the present work, constant α values are associated with elliptic curves, whereas constant β values result in lines joining the two walls (see Fig. 1(b)). In this case, the dimensionless boundary conditions are

$$T = 1, \quad \psi = 0 \quad \text{for } \alpha = \alpha_1 \text{ (inner wall)}, \tag{19}$$

$$T = 0, \quad \psi = 0 \quad \text{for } \alpha = \alpha_2 \text{ (outer wall)}, \tag{20}$$

and, since flow symmetry with respect to the vertical centre-plane is assumed,

$$\frac{\partial T}{\partial \beta} = 0, \quad \psi = 0, \quad \frac{\partial^2 \psi}{\partial \beta^2} = 0 \quad \text{for } \beta = \beta_1 \text{ and } \beta_2. \tag{21}$$

The second boundary condition on ψ is due to the fact that $\partial v_\alpha / \partial \beta = 0$ along the vertical symmetry plane. The dimensionless local heat flux at the wall is

$$q = \frac{R_1 q'}{k_e (T_1 - T_2)} = -\frac{1}{h_\alpha}\frac{\partial T}{\partial \alpha}. \tag{22}$$

At steady state, the dimensionless total heat flow across the annulus per unit axial length is

$$Q = \frac{Q'}{k_e (T_1 - T_2)} = -2\int_{\beta_1}^{\beta_2} \frac{h_\beta}{h_\alpha}\left(\frac{\partial T}{\partial \alpha}\right) \mathrm{d}\beta \quad \text{for } \alpha = \alpha_1 \text{ or } \alpha_2. \tag{23}$$

The global Nusselt number is defined as the ratio between the total heat flow and the heat flow when there is no convection ($Ra = 0$):

$$Nu = \frac{Q_{\text{total}}}{Q_{\text{conduction}}} = \frac{Q}{2(\beta_2 - \beta_1)}\int_{\alpha_1}^{\alpha_2} \left(h_\alpha / h_\beta\right) \mathrm{d}\alpha. \tag{24}$$

3. Solution procedure

3.1. Numerical grid generation

It is very possible that an analytical orthogonal coordinate transformation exists for the geometry under study. For example, eccentric cylinders can be described by bipolar coordinates [1,2,7], whereas confocal elliptic cylinders can be handled by elliptic cylindrical coordinates [10,20,23]. In both cases the coordinate transformations are simple and lead to compact

expressions of the metric coefficients. However, the latter coordinate system restricts the annular geometry to being confocal, thus eliminating geometries of practical relevance such as those in which one of the walls is cylindrical. One of the goals of this work is to develop a code take can handle an arbitrarily shaped annulus, which means that the grid must be constructed numerically. The grid generation technique employed here is the orthogonal trajectory method [24]. An example of a numerical grid generated using this method is depicted in Fig. 1(b).

The orthogonal trajectory method, which is discussed in [25–27], is essentially a method of characteristics. It can be pictured as a two-step process. The first step is to lay down a family of smooth non-overlapping curves covering the computational domain, which define one of the computational coordinates. For the geometry under study an obvious choice is the family of elliptic curves defined by the following parametric equation:

$$x(\alpha,\theta)=B\cos\theta,\quad y(\alpha,\theta)=y_0+A\sin\theta, \tag{25}$$

where

$$A=A_1+(A_2-A_1)\alpha^*,\quad B=B_1+(B_2-B_1)\alpha^*,\quad \text{and}\quad y_0=\epsilon(1-\alpha^*) \tag{26}$$

are linear stretching transformations of

$$\alpha^*=\frac{(\alpha-\alpha_1)}{(\alpha_2-\alpha_1)}. \tag{27}$$

By varying the value of θ between $-\pi/2$ and $\pi/2$, each line identified by a constant α value defines an ellipse in the physical domain (half the annular space). The coordinate system (α,θ) is non-orthogonal, but the α coordinate already fulfils some of the required conditions: the curves defined by constant α values are orthogonal to the vertical symmetry plane and those defined by $\alpha=\alpha_1$ and $\alpha=\alpha_2$ match the wall boundaries of the annular space. The stretching transformations defined by Eqs. (26) and (27) give rise to uniformly spaced α-coordinate lines in the physical domain. By modifying those equations it is easy to create a non-uniform grid in the physical domain, e.g., to condense the α grid lines near wall boundaries.

The second step of the orthogonal trajectory method is to keep the α-coordinate lines and to replace the θ-lines by a set of orthogonal β-coordinate lines. In order to create the β-coordinate lines, a series of curves have to be constructed starting at prescribed points on one of the wall boundaries, ending at the other boundary, and intersecting each intervening α-coordinate line at right angles.

The slope of a constant α-coordinate line can be expressed as

$$\left(\frac{\mathrm{d}y}{\mathrm{d}x}\right)_{\alpha=\text{const}}=\frac{\partial y/\partial\theta}{\partial x/\partial\theta}. \tag{28}$$

For a trajectory to be orthogonal to this line, its slope must be

$$\left(\frac{\mathrm{d}y}{\mathrm{d}x}\right)_{\beta=\text{const}}=-\frac{1}{(\mathrm{d}y/\mathrm{d}x)_{\alpha=\text{const}}}=-\frac{\partial x/\partial\theta}{\partial y/\partial\theta}. \tag{29}$$

Furthermore, along such a line

$$\left(\frac{\mathrm{d}x}{\mathrm{d}\alpha}\right)_{\beta=\text{const}}=\frac{\partial x}{\partial\alpha}+\frac{\partial x}{\partial\theta}\left(\frac{\mathrm{d}\theta}{\mathrm{d}\alpha}\right)_{\beta=\text{const}},\qquad \left(\frac{\mathrm{d}y}{\mathrm{d}\alpha}\right)_{\beta=\text{const}}=\frac{\partial y}{\partial\alpha}+\frac{\partial y}{\partial\theta}\left(\frac{\mathrm{d}\theta}{\mathrm{d}\alpha}\right)_{\beta=\text{const}}. \tag{30}$$

Equating Eq. (29) and the ratio of the two expressions in Eq. (30) produces an ordinary differential equation defining the β-coordinate lines:

$$\left(\frac{\mathrm{d}\theta}{\mathrm{d}\alpha}\right)_{\beta=\text{const}}=-\frac{\left(\frac{\partial x}{\partial\alpha}\right)\left(\frac{\partial x}{\partial\theta}\right)+\left(\frac{\partial y}{\partial\alpha}\right)\left(\frac{\partial y}{\partial\theta}\right)}{\left(\frac{\partial x}{\partial\theta}\right)^2+\left(\frac{\partial y}{\partial\theta}\right)^2}. \tag{31}$$

The initial condition for this equation is the prescribed grid distribution on one of the wall boundaries. This non-stiff ODE is solved by an explicit fourth-order Runge–Kutta method [28]. Preliminary tests showed that for the geometries considered in this study the best grids are obtained by specifying the location of the β-coordinate lines on the outer wall and employing Eq. (31) to compute the trajectories towards the inner wall. The following grid distribution on the outer wall boundary ($\alpha=\alpha_2$) was employed:

$$x=B_2\cos\beta^*,\qquad y=A_2\sin\beta^*,\quad \beta^*=\pi\left(\frac{\beta-\beta_1}{\beta_2-\beta_1}-\frac{1}{2}\right). \tag{32}$$

If the numerical grid has M points in the α direction and N points in the β direction, it is convenient to set $\alpha_1=1$, $\alpha_2=M$, $\beta_1=1$, $\beta_2=N$, and employ unit grid spacing in both computational coordinates, since this leads to the simplest form of the finite-difference expressions.

3.2. Numerical method

The steady-state solution of the problem is computed using a more accurate scheme than those employed in our previous studies on concentric and eccentric cylinders [7–9]. In the present code, all de-

rivatives with respect to the computational coordinates, including those appearing in the definition of the metric coefficients, are computed using a fourth-order accurate compact differencing scheme described by Hirsh [29]. This author and Orszag and Israeli [30] credited the scheme to Kreiss [31]. The reader is also referred to Rubin and Khosla [32] for related methods.

Compact differencing employs implicit formulas relating both the functional value and the corresponding derivative at the node and its neighbours. Compact schemes have higher order accuracy than finite differences based on the same number of grid points. The increased order in accuracy comes at the expense of treating the derivatives at the grid points as unknowns.

If F and S are, respectively, the first and second derivatives of a continuous function $\phi(x)$, they can be approximated to fourth order on a uniform mesh by the following relations [29]:

$$(F_{i-1} + 4F_i + F_{i+1}) = \left(\frac{3}{\Delta x}\right)(\phi_{i+1} - \phi_{i-1}), \tag{33}$$

$$(S_{i-1} + 10S_i + S_{i+1}) = \left(\frac{12}{\Delta x^2}\right)(\phi_{i-1} - 2\phi_i + \phi_{i+1}). \tag{34}$$

These two equations yield a tridiagonal matrix for the solution of F or S, which can be easily solved by the Thomas algorithm if ϕ is known at the grid points. When the boundary values of F and/or S are unknown, the following fourth-order relationship, proposed by Hirsh [29], can be used to generate the additional boundary conditions:

$$\phi_i - \phi_{i+1} + \Delta x\left[KF_i + (1-K)F_{i+1}\right] + (\Delta x^2/2)\left[\left(K - \frac{1}{3}\right)S_i + \left(K - \frac{2}{3}\right)S_{i+1}\right] = 0. \tag{35}$$

Certain values of the free parameter K result in very handy relations: choosing $K = 1$ or $K = 0$ isolates the first derivative at a point; $K = 1/3$ or $K = 2/3$ isolate the second derivative.

Although the steady-state solution of the problem is sought, the transient term in Eq. (15) is retained in order to solve the equation by marching in fictitious time with an alternating direction implicit (ADI) method to reach the asymptotic solution. The split form of the algorithm proposed by Peaceman and Rachford [33], and adopted in one of our previous studies [7], is used here. A similar approach has been taken by Hirsh [2] to solve 2D low Reynolds number viscous steady flows in a fluid layer. The two approaches differ, however, in the method for solving the elliptic Poisson Eq. (16) for the stream function.

In each iteration ($n \rightarrow n+1$), new temperature values are computed by applying one step of the ADI method to Eq. (15) using the most recently calculated values of the stream function, ψ^n. Since the compact difference scheme treats both the functional values and the derivatives as unknowns, each half-step of the ADI method requires the solution of a 3×3 block-tridiagonal matrix for each grid line in the implicit direction. These linear systems are solved efficiently by a block-extension of the Thomas algorithm [34]. Boundary values of T and of its derivatives at the ends of each line being solved are obtained from the boundary conditions of the problem and, when necessary, from Eq. (35).

After completion of a full ADI step, the stream-function values are updated using the following iterative procedure:

$$A \cdot \delta\psi^{n+1,\,k+1} = Ra \cdot b^{n+1} - \mathscr{L}\left(\psi^{n+1,\,k}\right), \tag{36}$$

$$\psi^{n+1,k+1} = \psi^{n+1,k} + \delta\psi^{n+1,k+1} \quad (k = 1, 2, \ldots), \tag{37}$$

where $\psi^{n+1,0} = \psi^n$, k is the inner iteration index, A is an iteration matrix, and $Ra \cdot b^{n+1}$ is the vector holding the values on the right-hand side of Eq. (16) computed at the grid points using compact differences on the updated temperature values, T^{n+1}. The operator $\mathscr{L}(\cdot)$ approximates the left-hand side of Eq. (16) by compact differences and depends only on the computational grid. The additional boundary conditions on ψ are obtained using Eq. (35).

The iteration matrix A is an approximate LU decomposition of the system of linear algebraic equations that is obtained by discretisation of the left-hand side of Eq. (16) using the standard three-point second-order central finite differences. The approximate LU decomposition is based on the Modified Strongly Implicit Procedure (MSIP) developed by Schneider and Zedan [35], which is itself an improvement over the Strongly Implicit Procedure of Stone [36]. The reader is referred to the original works for further details on the decomposition procedure. MSIP has a relaxation parameter, τ, in order to increase the convergence rate. Preliminary tests revealed that, in general, the best convergence rate for our problem is obtained with $\tau = 0.7$.

Since the iteration matrix A depends only on the grid, the approximate LU decomposition of A is performed only once, prior to the start of the main calculations. Once this has been done, each iteration given by Eq. (36) is computed efficiently because A has already been factored into a lower L and upper U triangular matrices. Although convergence can not be proved for all cases, extensive testing demonstrated

that the iterative procedure devised works well in practice.

The whole scheme is repeated until the solution converges. The calculations are ended when, for every grid point, the dimensionless temperature difference between two consecutive time steps is smaller than a prescribed tolerance, TOL, which is proportional to Δt:

$$\max_{i,j} |T_{i,j}^{n+1} - T_{i,j}^{n}| < \mathrm{TOL}, \quad \mathrm{TOL} = 10^{-4}\Delta t. \tag{38}$$

Fictitious time steps in the range $10^{-1} - 10^{-3}$ were employed in practice.

A computational grid with 161×101 ($\alpha \times \beta$) points covering half the annular space was employed, since symmetry with respect to the vertical centre-plane is assumed. Based on our previous work [7–9] the grid is probably over-sized for the accuracy intended. However, the grid dimensions were not reduced because the computational time was relatively short (less than 20 min) and we wanted to ensure that multicellular flow structures were captured with high resolution. Furthermore, the Péclet number based on grid spacing for this mesh was always below 2 for the various cases considered, ensuring that the matrix A employed in the stream-function iterative procedure was always diagonally dominant.

Due to the implicit nature of compact differences, the local temperature gradients in the α direction on both walls are readily available, since they are computed to fourth order as part of the solution. The global Nusselt number is calculated using a numerical quadrature procedure compatible to fourth-order accuracy [28]. The difference in the calculated Nusselt numbers for the inner and outer walls was never greater than 0.5%.

Table 1
Comparison of values of Nusselt number obtained using compact finite differences (present work) with values obtained numerically by other authors[a]

Ra	Padé	Fourier–Galerkin	Collocation–Chebyshev	Finite differences	Present work
Two-cellular flow $\epsilon \leq 0.001$					
50	1.343			1.335	1.338
100	1.862			1.844	1.861
120		2.050	2.052		2.050
150	2.26			2.26	2.309
200	2.54	2.68	2.684	2.63	2.688
300		3.287	3.310		3.322
$\epsilon = 0.2$					
50	1.293			1.288	1.292
100	1.765			1.743	1.764
200	2.59			2.462	2.550
$\epsilon = 0.4$					
50	1.246				1.247
100	1.62			1.61	1.621
150	1.98			1.95	1.975
200	2.3			2.26	2.294
$\epsilon = 0.6$					
50	1.199				1.198
100	1.479			1.465	1.479
150	1.744			1.69	[b]
200	1.993			1.93	[b]
$\epsilon = 0.8$					
50	1.143				1.144
100	1.327			1.32	1.327
150	1.494			1.47	1.500
200	1.64			1.62	1.642
Four-cellular flow, $\epsilon = 0$					
120		2.266	2.261		2.272
200		2.90	2.907		2.921
300		3.48–3.56	3.55–3.70		3.520

[a] Padé: Ref. [2]; Fourier–Galerkin and collocation–Chebyshev: Ref. [6]; finite differences: Ref. [18].
[b] Our numerical analysis revealed that only the four-cellular solution is stable.

4. Code validation

In order to ascertain the validity of the code, preliminary runs were made for several test cases and the results were compared with those reported by other authors. The comparison is limited to concentric and eccentric cylinders, since these are the only geometries for which information is available in the existing literature. However, since changing the eccentricity factor gives rise to noticeable differences in the overall shape of the annular space, this approach is sufficient to test the validity and accuracy of the grid generation technique and numerical solver.

Table 1 compares steady-state global Nusselt numbers obtained using the present code with those reported by other authors using different numerical techniques [2,8,18]. The comparison covers a large range of ϵ and Ra values, and includes both two- and four-cellular two-dimensional flow regimes. The present results are shown to be in good agreement with those obtained using other numerical techniques. In particular, our Nusselt numbers are much closer to those obtained using the Padé and Galerkin methods than the results of the low-order finite differences. This fact suggests that the present results are, indeed, computed with higher accuracy.

As a further test of the accuracy of our code, the critical Rayleigh number for the onset of the 2D four-cellular flow regime was determined for a concentric porous annulus of radius ratio $R = 2$. This case has received the most attention in the literature, both experimentally and numerically [3,6,8,9,12]. In order to determine the bifurcation point, the lower branch of the Nusselt curve, identifying the two-cellular flow, was first obtained by computing the steady-state solution for successively larger values of the Rayleigh number. Each calculation was run using the previously converged solution as the initial condition. The initial guess for the smallest Rayleigh number considered was the steady-state solution of the pure conduction regime.

If desired, the code can perturb the initial conditions in order to induce the appearance of a multicellular flow regime. However, in most cases a four-cellular flow solution can be obtained from an initial condition representing a two-cellular flow if the increment on Ra is large enough. This applies to both cylindrical and elliptical geometries.

As soon as the transition to a four-cellular flow occurred, either spontaneously or by perturbing the initial conditions, the calculations were carried out in inverse order, i.e., for decreasing Rayleigh numbers (upper branch of the Nusselt curve). The process was repeated until the flow became two-cellular again.

According to our numerical results, the critical Rayleigh number for the transition from the two- to the four-cellular flow regime is

$$62.95 < Ra_c < 63.00. \tag{39}$$

This value is lower than both our previous estimate ($Ra_c \approx 67 \pm 0.5$) based on a second-order finite difference code [8,9] and the value obtained by Rao et al. [3] using the Galerkin method at low approximation ($Ra_c = 65.5 \pm 0.5$). However, our higher-order estimate is very close the value obtained by Himasekar and Bau [5] using a linear stability analysis ($Ra_c \approx 62$) and to the value obtained by Charrier-Mojtabi [12] using a method based on a mixed Fourier–Chebyshev approximation ($60.5 < Ra_c < 61.5$). Notice that if the grid is not too coarse, increasing the order of the numerical solution procedure is equivalent to increasing the grid resolution for a lower order method. Thus, a lower estimate of Ra_c is consistent with an increase in accuracy of the numerical solution because it has been demonstrated [8,9] that a coarse grid is the reason why some authors do not obtain multicellular flows.

In view of the comparisons presented above we have every reason to believe that our code is capable of solving the two-dimensional Darcy–Boussinesq equations in generalised coordinates with high accuracy.

5. Results and discussion

The results given here are limited to a single Rayleigh number of 100 and to a hydraulic radius ratio $R = 2$. Performing a detailed analysis of all parameters (Ra, R, ϵ, Ω_1, and Ω_2) would certainly represent too much information to include in a single study. Since the novelty in this work is clearly the geometry and since the influence of Rayleigh number in porous annuli has already been studied extensively by several authors [6–12], we prefer focusing on the geometric parameters to including results for several values of Ra and R.

A Ra number of 100 is large enough for convective effects to prevail over conduction and for the appearance of multicellular flow patterns in many geometries. The two-dimensional four-cellular flow regime has been observed experimentally [6] for $Ra > 69$ in a concentric cylindrical annulus of $R = 2$. Under those flow conditions, the total heat transfer calculated numerically for moderate values of the Rayleigh number ($Ra < 140$) compares well with the average heat transfer measured experimentally when the flow is already three dimensional (e.g., Fig. 6 of Ref. [8]). For this range of Rayleigh numbers, the heat transfer calculated numerically in four-cellular flow conditions is closer to the experimental 3D flow data than that obtained with a two-cellular flow field [9]. By selecting $Ra = 100$ and $R = 2$, the present study addresses con-

ditions for which both the two- and four-cellular two-dimensional flows are physically possible and allows some extrapolation of the predicted heat transfer data to three-dimensional flow. Furthermore, since fixing the hydraulic radius ratio is equivalent to comparing annuli with the same cross-section area, the impact on heat transfer of reshaping the same amount of insulating material can be assessed. This is particularly useful in minimising the heat losses in annular porous insulation.

The results obtained for concentric annuli are presented first. Fig. 2 shows the impact on total heat flow of changing the shape of one of the annular walls. The same heat transfer data are plotted as Nusselt numbers in Fig. 3. In order to separate the effect of the geometry of each wall, the results depicted in the two figures do not include annuli for which both walls are elliptical. The subscript in Ω_i ($i = 1$ or 2) indicates which wall has elliptic shape, the other wall being cylindrical. Thus, Figs. 2 and 3 are essentially plots of the total heat loss (or Nusselt number), for the same amount of porous material, as a function of varying the elliptic shape of a single wall.

Notice that Ω_i ($\Omega_i > 1$) and $1/\Omega_i$ are instances of the same geometry. The difference between them is that for Ω_i the major axis of wall i is horizontally aligned, whereas for $1/\Omega_i$ the major axis is vertically aligned. Therefore, two annuli characterised by Ω_i and $1/\Omega_i$ only differ in their orientation with respect to the gravity field. Each pair of these geometries is easily identified in Figs. 2 and 3 by the values $\pm \ln \Omega_i$.

According to Fig. 2, if in the range $-0.5 < \ln \Omega_i < 0.3$ the same rate of deformation is applied either to the inner or to the outer wall of the annular space, then identical values of the total heat transfer are obtained in the two-cellular flow regime. This is an unexpected observation, considering that the two geometries give different heat transfer rates under pure conduction conditions ($Ra = 0$). This is why the same heat transfer data when plotted in the form of Nusselt number do not appear as two superposed curves in Fig. 3. The range of values of $\ln \Omega$ for which the two heat transfer curves are coincident extends further to negative values (vertical stretching of one of the cylinders) than to positive ones (horizontal stretching). As depicted in Fig. 2, Q varies linearly with $\ln \Omega$ under those conditions.

Since the results of Fig. 2 refer to annuli of hydraulic radius ratio $R = 2$, as $|\ln \Omega_i| \to 4$ the total heat flow tends to infinity and the overall Nusselt number plotted in Fig. 3 approaches one. The prevailing mechanism influencing the heat transfer rate across an annulus with a highly deformed wall is the straightening of the local thickness of the layer, regardless of occurring vertically or laterally. Its ultimate effect is to increase the total heat flow, as shown by the increasing trend of the Q curves in the edges of the graph of Fig. 2.

The total heat transfer under two-cellular flow conditions is always increased with vertical wall stretching ($\ln \Omega < 1$). If a cylindrical wall is, however, moderately flattened in the horizontal direction ($0 < \ln \Omega < 0.3$),

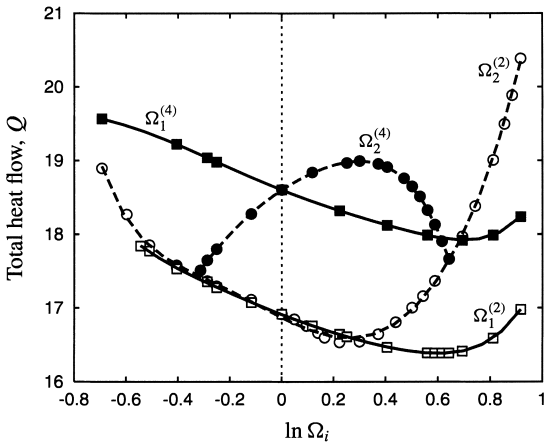

Fig. 2. Dimensionless total heat flow (Q) in a concentric elliptic annulus as a function of the axis ratio (Ω_i) for $Ra = 100$ and $R = 2$. The numerical results (symbols) have been line-fitted in order to give a better visualization of the trends. The subscript in Ω_i identifies the elliptic wall [1 = inner (squares), 2 = outer (circles)], the other wall being a cylinder; the integer superscript characterises the flow regime with respect to the number of convective cells [2 = two-cellular flow (open symbols), 4 = four-cellular flow (solid symbols)].

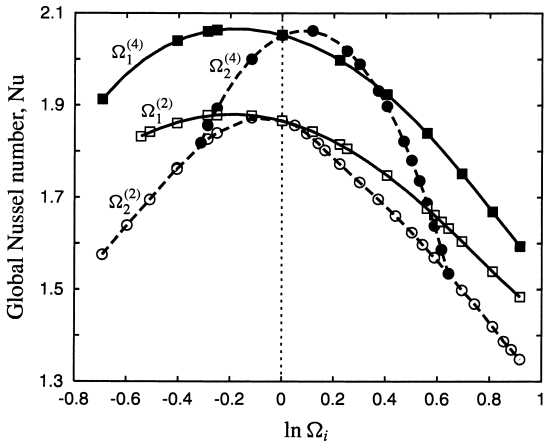

Fig. 3. Global Nusselt number (Nu) in a concentric elliptic annulus as a function of the axis ratio (Ω_i) for $Ra = 100$ and $R = 2$. The numerical results (symbols) have been line-fitted in order to give a better visualization of the trends. The nomenclature is the same as that employed in Fig. 2.

then the total heat flow decreases. Further stretching of the outer ellipse horizontally leads to a steep increase of the total heat transfer, the cause is explained below. This behaviour is not observed when the same rate of deformation is applied to the inner wall; in this case, the total heat flow maintains a decreasing trend until $\ln \Omega_2 \approx 0.6$, where the minimum heat flow is obtained, and then increases with further stretching of the wall.

Fig. 4 depicts streamlines and isotherms in the two-cellular flow regime for geometries illustrating the various annuli addressed in Figs. 2 and 3. Isotherms and streamlines under four-cellular flow conditions for annuli with similar shapes as those of Fig. 4 are plotted in Fig. 5. An unexpected flow regime obtained numerically is that of Fig. 4(d), it differs from the usual four-cellular flow pattern depicted in Fig. 5(d). This unusual flow regime appears for $\ln \Omega_2 > 0.3$ (outer wall horizontally flattened) and is characterised by the fact that the secondary cell in each half-annulus is enfolded by the main cell and is co-rotating, whereas the secondary cell in Fig. 5(d) is segregated from the main cell and is counter-rotating. The numerical results show that this flow regime is stable and that it prevails over the two-cellular flow, however only experimental evidence can ascertain if it is physically possible. The appearance of the co-rotating cell and the reduction of local gap width in the top part of the porous layer explain the detachment of the heat transfer curve from that of Fig. 4(b), causing a steep increase in Q (open circles in Fig. 2).

The numerical results show that the judicious stretching of one of the cylinders in the horizontal direction reduces the heat flow with respect to a concentric cylindrical annulus ($\ln \Omega_i = 0$) with the same radius ratio. Bau [1,2] and Mota and Saatdjian [7] showed that eccentric cylinders may be more effective insulation under certain conditions than concentric ones. The results presented here provide an alternative approach to optimising the heat transfer rate by a proper choice of the annular shape.

From the various options presented in Fig. 2, the lowest heat transfer rate in two-cellular flow conditions is obtained by flattening the inner wall horizontally (Fig. 4(b)). There are several factors that contribute to reducing the heat transfer in this case, which for moderate values of $\ln \Omega$ prevail over the opposing effect of decreasing the gap width between walls laterally. The first is that, although the center of the flow cell (the location of $|\psi_{\max}|$) is shifted upwards and positioned above the inner ellipse where the convective effects are more important, the re-circulation flow rate is not increased in that zone. In fact, $\psi_{\max}$ is smaller for $\ln \Omega_1 = 0.6$ ($\psi_{\max} = 8.44$) than for the case of two concentric cylinders ($\Omega_1 = \Omega_2 = 1$, $\psi_{\max} = 9.97$). This means that the convective heat transfer is not enhanced. Since the hori-

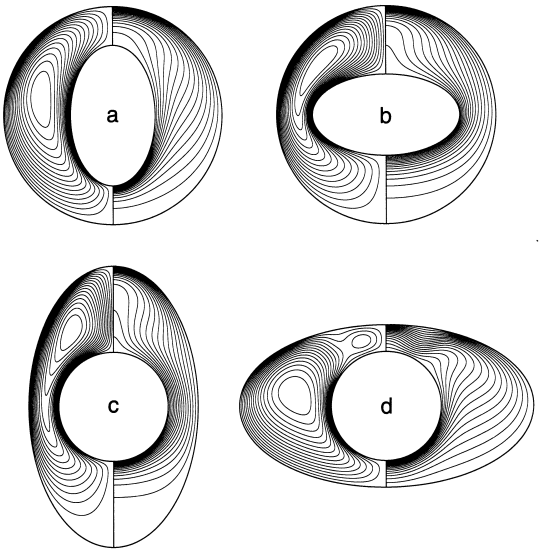

Fig. 4. Streamlines and isotherms in the two-cellular flow regime for $Ra = 100$, $R = 2$, and different concentric geometries ($\epsilon = 0$). (a) $\ln \Omega_1 = -0.5$, $\Omega_2 = 1$; (b) $\ln \Omega_1 = 0.6$, $\Omega_2 = 1$; (c) $\Omega_1 = 1$, $\ln \Omega_2 = -0.5$; (d) $\Omega_1 = 1$. $\ln \Omega_2 = 0.6$. The streamlines and the isotherms occupy the right- and left-hand sides of each annulus, respectively.

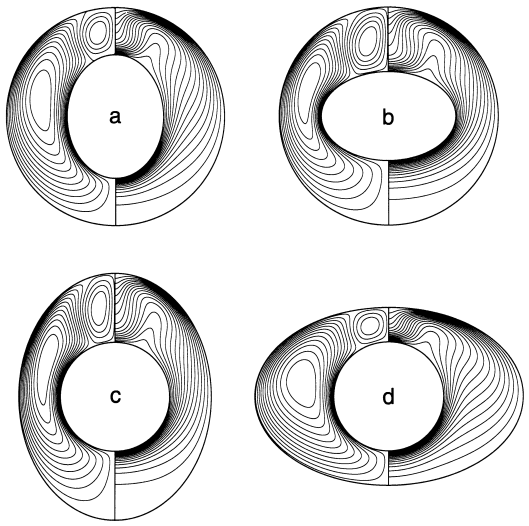

Fig. 5. Streamlines and isotherms in the four-cellular flow regime for $Ra = 100$, $R = 2$, and different concentric geometries ($\epsilon = 0$). (a) $\ln \Omega_1 = -0.25$, $\Omega_2 = 1$; (b) $\ln \Omega_1 = 0.4$, $\Omega_2 = 1$; (c) $\Omega_1 = 1$, $\ln \Omega_2 = -0.25$; (d) $\Omega_1 = 1$, $\ln \Omega_2 = 0.4$. The streamlines and the isotherms occupy the right- and left-hand sides of each annulus, respectively.

zontal stretching of the inner wall increases considerably the local thickness of the top part of the layer (Fig. 4(b)) the conductive heat losses are reduced. Similarly, in the stagnant region located below the inner wall, the local thickness of the layer is also increased with horizontal wall stretching, and reduces the conductive heat transfer prevailing in that zone. In the lateral zones, where the porous layer is thinner, the fluid moves parallel to the walls due to the core region between the two hydrodynamic boundary layers being very thin. This gives rise to locally concentric isotherms, which are nearly uniformly spaced, resulting in a low temperature gradient in that part of the layer, and moving to stronger deformations the prevailing effect of local thickness straightening.

As expected, when the flow changes to a four-cellular regime the heat transfer is enhanced. The increase in total heat flow is of about 10%. Stretching the inner wall makes the total heat flow curve behave as if the two-cellular heat transfer curve had been shifted upwards on the vertical axis of Fig. 2. If the outer cylinder is stretched, the shape of the resulting heat transfer curve is inverted with respect to the other heat transfer curves. It is also observed that stretching the outer cylinder significantly, either horizontally or vertically, hinders the appearance of the four-cellular flow regime. With vertical stretching of the outer wall, the local thickness of the top part of the layer increases and the secondary counter-rotating cell is squeezed horizontally against the vertical symmetry axis by the main cell (Fig. 5(c)) and eventually disappears. The resulting effect is a decrease in heat transfer. If, on the other hand, an initially cylindrical outer wall is slightly stretched horizontally, the heat flow increases due to the decrease of gap width in the top part of the layer. Further stretching shrinks the counter-rotating cell due to the conical shape of the top part of the layer (Fig. 5(d)) and reduces the heat transfer.

If the four-cellular flow pattern prevails in the layer, the minimum of the heat flow curve is located at $\ln \Omega_2 = -0.3$, which means that the best way to minimise the heat losses in this flow regime is to vertically stretch the outer wall until the two counter-rotating cells disappear. The improvement obtained over flattening the outer wall horizontally in order to achieve the same effect is, nevertheless, small. For $Ra = 100$ and $R = 2$, when the outer wall is horizontally stretched by just the amount required to eliminate the counter-rotating cells, the resulting geometry also gives, curiously, the minimum heat transfer in the two-cellular flow regime. Thus, from the geometries covered in Fig. 2 the choice $\ln \Omega_1 = -0.6$ and $\Omega_2 = 1$ is clearly the best option to minimise the heat losses in both flow regimes.

The heat transfer rate can be optimised further if the concentric geometry that gives the minimum heat flow is made eccentric. The results are depicted in Fig. 6, which shows the variation of both total heat flow and global Nusselt number as a function of the relative eccentricity, ϵ. As depicted in Fig. 6, the heat transfer in both two- and four-cellular flow conditions shows a steep increase for large negative values of ϵ, which is coincident with the enlargement of gap width in the top part of the layer. For positive values of ϵ, the heat flow curve in four-cellular flow is insensitive to the eccentricity until $\epsilon \approx 0.8$, where the top layer becomes so thin that the counter-rotating cells disappear. The minimum heat transfer in two-cellular flow conditions is obtained for $\epsilon = 0.4$. Streamlines and isotherms for this geometry in both flow regimes are plotted in Fig. 7. Since for this geometry, the heat transfer in four-cellular flow does not increase compared to the same flow conditions in the concentric case, this eccentric geometry is a good choice if one wishes to minimise the heat transfer in both flow regimes. The savings in heat loss is of about 10%.

We also plot in Fig. 8 the effect of eccentricity on the total heat flow and global Nusselt number for the geometry that gives the maximum heat transfer rate in four-cellular flow conditions, i.e., $\Omega_1 = 1$ and $\ln \Omega_2 \approx 1/3$ (maximum of the curve represented by solid circles in Fig. 2). The results show that the savings in two-cellular flow conditions for this geometry can not be improved by varying the eccentricity, and are only marginally decreased ($\approx 2\%$) with respect to two concentric cylinders. However, in four-cellular flow conditions the heat transfer can be reduced by

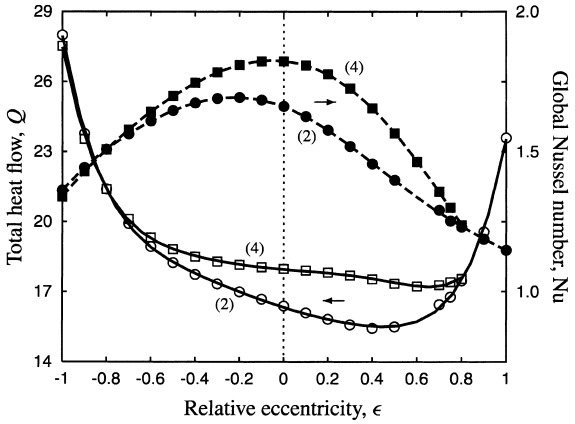

Fig. 6. Dimensionless total heat flow (Q) and global Nusselt number (Nu) as a function of eccentricity (ϵ) for $Ra = 100$, $R = 2$, $\ln \Omega_1 = 0.6$ and $\Omega_2 = 1$. The heat transfer data (symbols) have been line-fitted in order to provide a better visualization of the trends. The open symbols represent the heat flow data, while the solid ones denote the Nusselt numbers. Circles: two-cellular flow; squares: four-cellular flow.

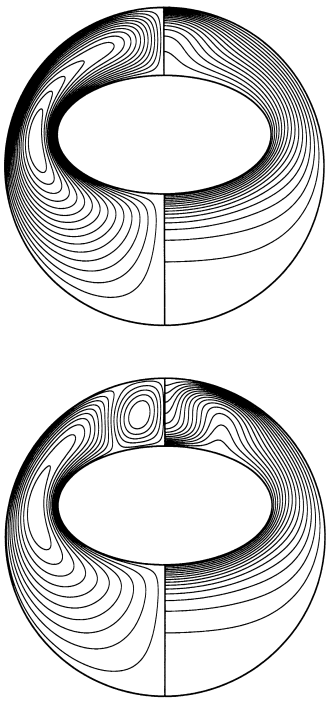

Fig. 7. Streamlines and isotherms for $Ra = 100$, $R = 2$, $\ln \Omega_1 = 0.6$, $\Omega_2 = 1$ and $\epsilon = 0.4$. The streamlines and the isotherms occupy the right- and left-hand sides of each annulus, respectively. Top annulus: two-cellular flow regime; bottom annulus: four-cellular flow regime.

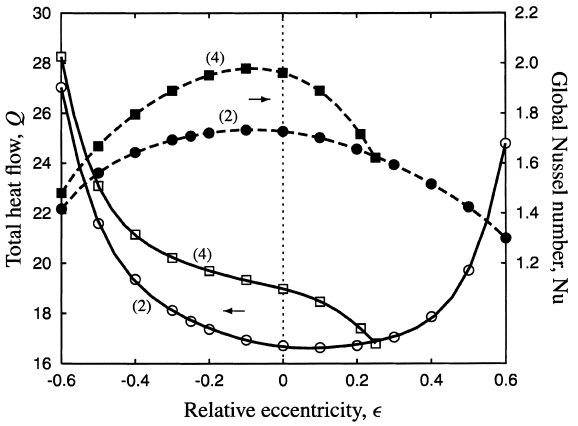

Fig. 8. Dimensionless total heat flow (Q) and global Nusselt number (Nu) as a function of eccentricity (ϵ) for $Ra = 100$, $R = 2$, $\Omega_1 = 1$, and $\ln \Omega_2 = 1/3$. The heat transfer data (symbols) have been line-fitted in order to provide a better visualization of the trends. The nomenclature is the same as that employed in Fig. 6.

about 10% compared to the concentric cylindrical geometry by a proper choice of the eccentricity. The gain can be considered even greater if the base of comparison is taken as the same elliptic geometry with $\epsilon = 0$. Once again, the optimum value of ϵ is the lowest value of ϵ for which the shape of the annulus eliminates the counter-rotating cells.

6. Conclusions

A very accurate and efficient code has been developed to solve the two-dimensional Darcy–Boussinesq equations, governing natural convection heat transfer in horizontal porous annuli. The equations are solved in generalised orthogonal coordinates using high-order compact finite differences and an ADI time-marching scheme. The mesh is generated numerically using the orthogonal trajectory method, thus the code can be easily used to investigate any annular geometry as long as the 2D assumptions hold. The code has been thoroughly validated against numerical results reported by other authors for concentric and eccentric cylindrical annuli.

In order to illustrate the potential of the code, it has been used to study natural convection heat transfer in eccentric elliptic porous insulation. The results clearly demonstrate that the heat losses can be minimised by a proper choice of the elliptic shape of a concentric annulus, which can be further enhanced if the geometry is made eccentric. Previous studies have shown that eccentric cylinders may be more effective insulation under certain conditions than concentric ones. Our findings provide an alternative approach of optimising the heat transfer rate by a proper choice of both the elliptic character and eccentricity of the annulus.

Acknowledgements

The financial support received from Faculdade de Ciências e Tecnologia da Universidade Nova de Lisboa (JD4/DQ/98) is gratefully acknowledged.

References

[1] H.H. Bau, Low Rayleigh number thermal convection in a saturated porous medium bounded by two horizontal eccentric cylinders, J. Heat Transfer 106 (1984) 166–175.
[2] H.H. Bau, Thermal convection in a horizontal eccentric annulus containing saturated porous medium — an extended perturbation expansion, Int. J. Heat Mass Transfer 27 (1984) 2277–2287.
[3] Y.F. Rao, K. Fukuda, S. Hasegawa, Steady and transient analyses of natural convection in a horizontal por-

ous annulus with the Galerkin method, J. Heat Transfer 109 (1987) 919–927.
[4] Y.F. Rao, K. Fukuda, S. Hasegawa, A numerical study of three-dimensional natural convection in a horizontal porous annulus with Galerkin method, Int. J. Heat Mass Transfer 31 (1988) 695–707.
[5] K. Himasekhar, H.H. Bau, Two-dimensional bifurcation phenomena in thermal convection in horizontal concentric annuli containing saturated porous media, J. Fluid Mech. 187 (1988) 267–300.
[6] M.C. Charrier-Mojtabi, A. Mojtabi, M. Azaiez, G. Labrosse, Numerical and experimental study of multicellular free convection in an annular porous layer, Int. J. Heat Mass Transfer 34 (1991) 3061–3074.
[7] J.P.B. Mota, E. Saatdjian, On the reduction of natural convection heat transfer in horizontal eccentric annuli containing saturated porous media, Int. J. Numer. Meth. Heat Fluid Flow 7 (1997) 401–416.
[8] J.P.B. Mota, E. Saatdjian, Natural convection in a porous horizontal cylindrical annulus, J. Heat Transfer 116 (1994) 621–626.
[9] J.P.B. Mota, E. Saatdjian, Natural convection in porous cylindrical annuli, Int. J. Numer. Meth. Heat Fluid Flow 5 (1995) 3–12.
[10] E. Saatdjian, R. Lam, J.P.B. Mota, Natural convection heat transfer in the annular region between porous confocal ellipses, Int. J. Numer. Meth. Fluids 31 (1999) 513–522.
[11] J.P. Caltagirone, Thermoconvective instabilities in a porous medium bounded by two concentric horizontal cylinders, J. Fluid Mech. 76 (1976) 337–362.
[12] M.C. Charrier-Mojtabi, Numerical simulation of two- and three-dimensional free convection flows in a horizontal porous annulus using a pressure and temperature formulation, Int. J. Heat Mass Transfer 40 (1997) 1521–1533.
[13] P.J. Burns, C.L. Tien, Natural convection is porous medium bounded by concentric spheres and horizontal cylinders, Int. J. Heat Mass Transfer 22 (1979) 929–939.
[14] K. Himasekhar, H.H. Bau, Large Rayleigh number convection in a horizontal eccentric annulus containing saturated porous media, Int. J. Heat Mass Transfer 29 (1986) 703–712.
[15] C.V. Raman, The theory of the Christiansen experiment, Proc. Ind. Acad. Sci. 29 (1949) 381–390.
[16] R.H. Clarke, A theory for Christiansen filter, Appl. Optics 7 (1968) 861–868.
[17] J.P. Caltagirone, Instabilités thermoconvectives en milieux poreux, Thèse d'Etat, Université Pierre et Marie Curie, Paris VI, France, 1976.
[18] H.H. Bau, G. McBlanc, I. Saferstein, Numerical simulation of thermal convection in an eccentric annulus containing porous media. ASME 32-WA/HT-34, 1983.
[19] A. Aniri, K. Vafai, Analysis of dispersion effects and non-thermal equilibrium, non-Darcian, variable porosity incompressible flow through porous medium, Int. J. Heat Mass Transfer 37 (1994) 939–954.
[20] J.H. Lee, T.S. Lee, Natural convection in the annulus between horizontal confocal elliptic cylinders, Int. J. Heat Mass Transfer 24 (1981) 1739–1742.
[21] A. Mojtabi, M.C. Charrier-Mojtabi, Analytical solution of steady natural convection in an annular porous medium evaluated with a symbolic algebra code, J. Heat Transfer 114 (1992) 1065–1067.
[22] C.A.J. Fletcher, in: Computational Techniques for Fluid Dynamics, 2nd ed., vol. II, Springer-Verlag, Berlin, 1991 (Chapter 13).
[23] G.D. Raithby, K.G.T. Hollands, Laminar and turbulent free convection from elliptic cylinders with a vertical plate and horizontal circular cylinder as special cases, J. Heat Transfer 98 (1976) 72–80.
[24] J.F. Thompson, Grid generation techniques in computational fluid dynamics, AIAA J. 22 (1984) 1505–1523.
[25] P.R. Eiseman, Orthogonal grid generation, in: J.F. Thompson (Ed.), Numerical Grid Generation, North-Holland, Amsterdam, 1982, pp. 193–234.
[26] P.R. Eiseman, Coordinate generation with precise controls over mesh properties, J. Computational Phys. 47 (1982) 331–351.
[27] P.R. Eiseman, High level continuity for coordinate generation with precise points, J. Computational Phys. 47 (1982) 352–374.
[28] W.H. Press, B.P. Flannery, S.A. Teukolsky, W.T. Vetterling, Numerical Recipes, Cambridge University Press, Cambridge, 1989.
[29] R.S. Hirsh, Higher order accurate difference solutions of fluid mechanics problems by a compact differencing technique, J. Computational Phys. 19 (1975) 90–109.
[30] S.A. Orszag, M. Israeli, Numerical solution of viscous incompressible flows, in: Annual Review of Fluid Mechanics, vol. 6, Annual Reviews, Palo Alto, CA, 1974.
[31] H. Kreiss, J. Oliger, Methods for the approximate solution of time dependent problems. GARP Publication Series No. 10, World Meteorological Organization, 1973. (Available from UNIPUB, Inc., P.O. Box 433, New York, NY 10016.).
[32] S.G. Rubin, P.K. Khosla, Polynomial interpolation methods for viscous flow calculations, J. Computational Phys. 24 (1977) 217–244.
[33] D.W. Peaceman, H.H. Rachford, The numerical solution of parabolic and elliptic differential equations, SIAM J. 3 (1955) 28–41.
[34] G.H. Golub, C.F. van Loan, Matrix Computations, 2nd ed., Johns Hopkins University Press, Baltimore, MD, 1989.
[35] G.E. Schneider, M. Zedan, A modified strongly implicit procedure for the numerical solution of field problems, Numer. Heat Transfer 4 (1981) 1–19.
[36] H.L. Stone, Iterative solution of implicit approximations of multidimensional partial differential equations, SIAM J. Numer. Anal. 5 (1968) 530–558.